Journal of Computational Applied Mechanics 2023, 54 (2): 236-253

DOI: 10.22059/jcamech.2023.351454.775

RESEARCH PAPER

Optimum design of a micro-positioning compliant mechanism based on neural network metamodeling

Erfan Norouzi Farahani [a], Niloofar Ramroodi [a], Maryam Mahnama [a,*]

[a] *School of Mechanical Engineering, College of Engineering, University of Tehran, Tehran, Iran*

Abstract

This paper presents a comprehensive investigation of the optimization process of a compliant micro-positioning mechanism based on a high-accuracy metamodel. Within this study, for the first time, analytical approach, finite element analysis (FEA), deep neural network (DNN), and particle swarm optimization (PSO) algorithm are integrated in order to achieve the optimum design of a parallel 2-degree-of-freedom compliant positioner while taking a broad range of factors into account. First, a linear regression analysis is performed on the primary finite element model as a sensitivity analysis. Then an analytical model is established to express one of the objective functions of design, namely the mechanism working range, as a function of characteristic features: the mechanism stiffness and displacement amplification ratio (λ). In the optimization procedure, a single objective-constrained PSO (SOCPSO) algorithm is implemented on the metamodel to maximize the resonant frequency and provide the minimum acceptable working range. The proposed optimization guideline is established for seven different desired working ranges and effective data selection leads to a great minimum accuracy of 97% between FEM and DNN with a relatively small dataset. In addition, the results show the principle resonant frequency of the proposed design is 327.5377 Hz, and the working range reaches over 118 μm in both axes with the cross-coupling less than 0.2%. The findings provide insights into the design and geometric optimization of mechanical structures. Furthermore, it will be employed as a guideline for implementing DNN for metamodeling in other engineering problems.

Keywords: Compliant mechanism; Finite Element Analysis (FEA); Metamodel; Deep Neural Networks (DNN); Single-Objective Constrained Particle Swarm Optimization (SOCPSO) algorithm;

1. Introduction

Piezoelectric actuators are widely used in precision positioning but have a limited range of motion, about 0.1%-0.2% of their length, which is insufficient for many applications and must be magnified [1-3]. It is also necessary to obtain a compressive preload to prevent damaging tensile stress in the piezoelectric stack [4]. Having the advantages of smooth and frictionless movement, no backlash [5, 6], high reliability, no need for assembly or lubrication [7, 8], and a compact monolithic structure [9], compliant mechanisms are the most accepted candidates to magnify

* Corresponding author. Tel.: +982161114019; fax: +98-2188013029.
E-mail address: m.mahnama@ut.ac.ir

piezoelectric strain by a factor called displacement amplification ratio in various applications such as scanning probe microscopy [10, 11], constant-force applications in biology [12], and micro grippers [13, 14].

Like any 2-D positioning system, compliant mechanisms are categorized into two main types, serial and parallel. Serial mechanisms usually consist of two nested 1-D positioners that are easy to design but have significant cumulative errors [15]. Also, these mechanisms have an unsymmetrical configuration in two axes, which causes different stiffness and dynamic characteristics in two directions [16, 17]. Even so, several researchers have used serial configuration mechanisms for scanning applications [18]. For instance, Wadikhaye et al. designed a compact serial-kinematic atomic force microscopy (AFM) scanner with a displacement range of $8\times 2\mu m^2$ and high first natural frequency [19]. Kenton et al. proposed an innovative design that ensured equal ranges for both in-plane axes. Despite this, the additional mass of the second axis reduced the corresponding natural frequency by 300% as compared with the first axis [20]. Parallel mechanisms have numerous advantages over serial counterparts, such as low inertia, high resonant frequency [21], and higher compatibility [6, 22]. However, their kinematics is nonlinear [23] and needs extra parts to decouple the motion of the two axes [24]. Compared to serial mechanisms, there are more studies on the parallel type. For example, Li et al. have presented an elaborated parallel piezo-actuated 2D stage with relatively high bandwidth and working range. Although, the authors noted that complex geometry had caused 4% crosstalk in two axes [25]. In another study, Jin et al. succeeded to reduce the crosstalk for a small working range to under 1% [15]. Many other researchers have manipulated different elements to decouple the motion of the two axes. The best effort for this purpose was reported in the work of Lee et al. [26], where two thin leaf springs are used in both axes of this mechanism, resulting in a cross-coupling of only 0.65%.

In micro-positioning stages, the resonant behavior of the compliant mechanism is usually the most limiting factor for loading speed compared to piezoelectric actuators that operate at high frequencies [18]. Tian et al. have shown that there is an inverse relationship between maximum working range and resonant frequency (or stiffness) [27]. In this regard, several researchers have proposed designs with high displacement and low frequency [23, 28] and vice versa [16]. Due to the intrinsic trade-off between the displacement amplification ratio and the resonant frequency, geometric optimization is an essential step in the design process. Different parts of a compliant mechanism should be tuned to achieve the most desirable pair of these two characteristic parameters. The traditional optimization method requires several time-consuming numerical analyses to evaluate the objective functions and find the best combination of parameters. As an alternative approach to accelerate the computational complexity, An artificial neural network is one of the most powerful metamodels which construct a simple relationship between the input parameters and the corresponding objective values in both shapes [29, 30] and topology optimization [31, 32].

Particle Swarm Optimization (PSO) is a technique inspired by the social behavior of bird flocking and fish schooling in search of food. This technique was initially designed and developed by Eberhart and Kennedy [33]. The prominent features of PSO are its easy implementation, robustness to control parameters, and computation efficiency compared with other existing heuristic algorithms such as genetic algorithm in a continuous problem. PSO can be applied to non-differentiable, non-linear, huge search space problems and gives better results with good efficiency [34, 35].

This paper elaborates on a novel optimization guideline for the geometric parameters of a parallel compliant mechanism. The optimization procedure entails combining three main sections: performing a sensitivity analysis on the finite element method (FEM) results, training a deep neural network (DNN) on the obtained dataset, and finally applying the particle swarm optimization (PSO) algorithm. The sensitivity analysis is performed by a linear regression approach in order to achieve a significant reduction in variations space. A DNN serves as a surrogate model of time-consuming FEM simulations and feeds the PSO algorithm, which is proposed to discover the optimal combination of compliant mechanism geometry.

2. Methodology

This section details the implementation of FEM and the analytical model for training a couple of DNNs to predict the optimal performance of the parallel compliant mechanism. Fig 1 illustrates the schematic of the proposed optimization guideline methodology involving four steps. As the first step, a linear regression sensitivity analysis is performed on the primary FEM results consisting of attribution of both the displacement amplification and the principle natural frequency as the outputs for the parallel compliant mechanism to its several geometric features. After filtering the negligible parameters, the analytical model defines the mechanism working range in terms of displacement amplification as well as the input stiffness. Then in the third step, the new dataset containing 460 consistent states is provided for extensive training of the DNNs. The PSO algorithm uses DNN metamodels to find the optimal geometric parameters that satisfy manufacturing constraints and have the highest possible resonance frequency within the desired working range.

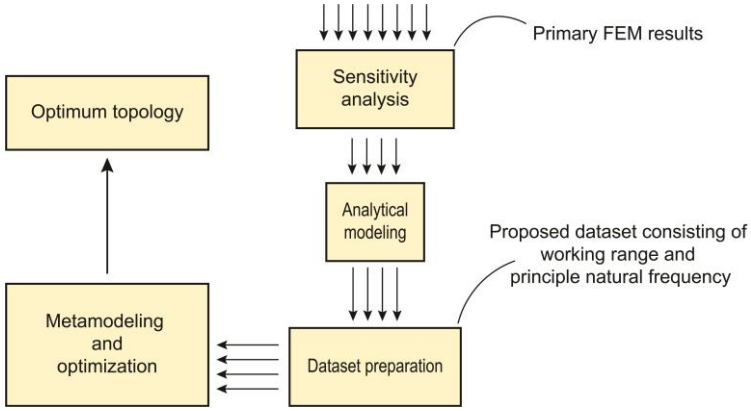

Fig 1: Flowchart of the proposed optimization guideline.

2.1. Finite Element Model

Configuration of the parallel model used in this paper [26] is shown in Fig 2 which consists of: (1) the inner stage, (2) six couple hinges which consist of prismatic beams and circular hinges, are used to suspend the inner stage at the center, (3) displacement amplifier sub-mechanisms to achieve a large working range due to the limited elongation of the actuator, (4) intermediate leaf springs, which enhance the stiffness in the transverse direction of the displacement amplifier, and (5) piezo stack as the actuator of the mechanism.

Due to the considerable difference between stiffnesses along the two orthogonal axes, the leaf springs act as an excellent motion decoupler and reduce the positioning error significantly. Therefore, the mechanism has low cross-coupling and yaw motion, which are related to the transverse and rotational stiffness. Cross-coupling is defined as the induced displacement along the transverse direction, and yaw is the motion generated by the rotation around the axis of motion. Circular hinges enhance the controllability of the mechanism.

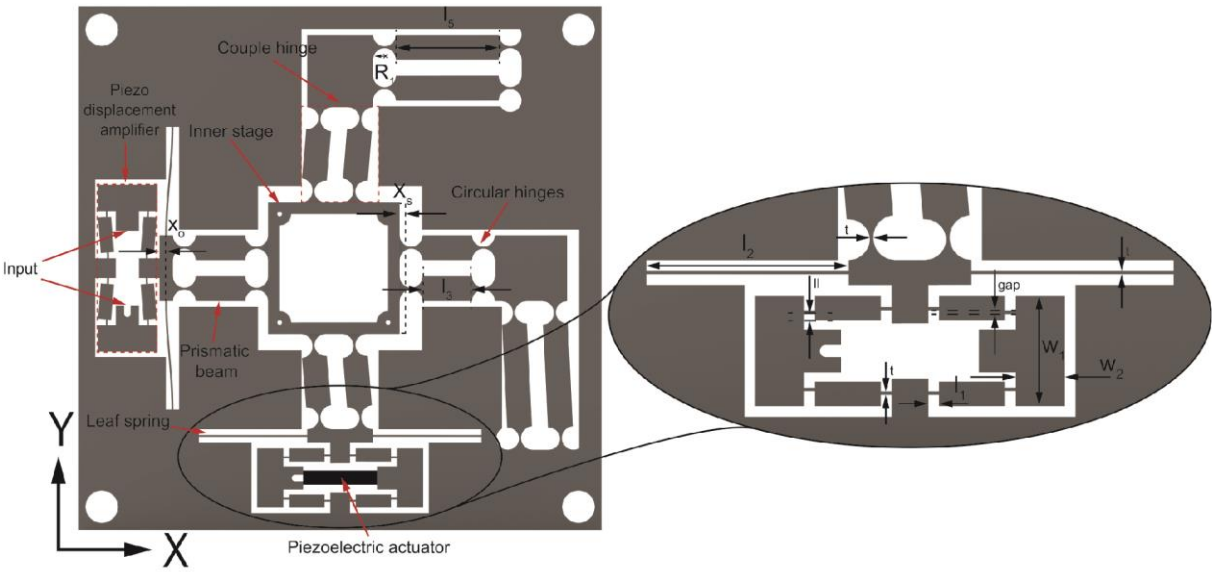

Fig 2: Schematic of different parts and geometric parameters of the parallel mechanism. Deformations have been shown magnified and one of the piezoelectric stacks has been omitted for more clarification.

The design of the compliant mechanism is performed in SolidWorks 2017 and considered based on Al 7075-T6 with Yong's modulus of $E = 71GPa$, shear modulus of $G = 27GPa$, and the density of $\rho = 2770kg.m^{-3}$. The tetrahedron element is used to construct 3D models generated by creating a live link to SolidWorks, and the multifrontal massively parallel sparse direct solver (MUMPS) in COMSOL modal analysis is imposed on the mechanism model without the piezoelectric actuator. The displacement amplification ratio is also defined as the proportion of displacement in the inner stage (X_S) to the piezoelectric displacement (x_S) (see Fig 5). A constant perpendicular force of 0.01 N on the inner stage represents measurement tools and the mechanism contact surfaces

with the screws fixed in all the FEM simulations. The modeling parameters of the piezo stack (free displacement (x_f) of 31 μm and blocking force (F_b) of 900 N) are adopted according to SA050520 model, which is a conventional actuator in experiments.

2.2. Sensitivity analysis and dataset preparation

It is noted that some of the parameters listed in Fig 2 will not be considered in the design dataset. Two main reasons can be enumerated for this fact: First, they have a negligible effect on the mechanism performance and only increase the difficulty of the optimization process, and second, they would likely create geometric incompatibility. Among all the geometric parameters, l_1, ll, and gap are tuned for achieving maximum displacement amplification ratio in amplifier sub-mechanism based on the study of Ma et al. [36].

In the next step, a linear regression method is utilized to evaluate the impact of $l_2, l_3, r_1, t, l_5, w_1, w_2$ parameters on the system performance to reduce the number of dimensions in the optimization problem. By changing the mentioned parameters, a set of 20 data points including the displacement amplification ratio (λ) and the mechanism resonant frequency (f) is prepared. The coefficients of α_i and β_i and the error terms (ε_1 and ε_2) in linear regression are calculated for seven input parameters (x_i) using equations 1 and 2, and participation quotes in both displacement amplification ratio and resonant frequency regressions are determined.

$$f = \alpha_0 + \sum_{i=1}^{7} \alpha_i x_i + \varepsilon_1 \tag{1}$$

$$\lambda = \beta_0 + \sum_{i=1}^{7} \beta_i x_i + \varepsilon_2 \tag{2}$$

Finally, the relative importance factors for λ and f is calculated using:

$$I_{j,f} = \frac{\sigma_{j,f}\alpha_j}{\sum_{i=1}^{7} \sigma_{i,f}\alpha_i} \tag{3}$$

$$I_{j,\lambda} = \frac{\sigma_{j,\lambda}\beta_j}{\sum_{i=1}^{7} \sigma_{i,\lambda}\beta_i} \tag{4}$$

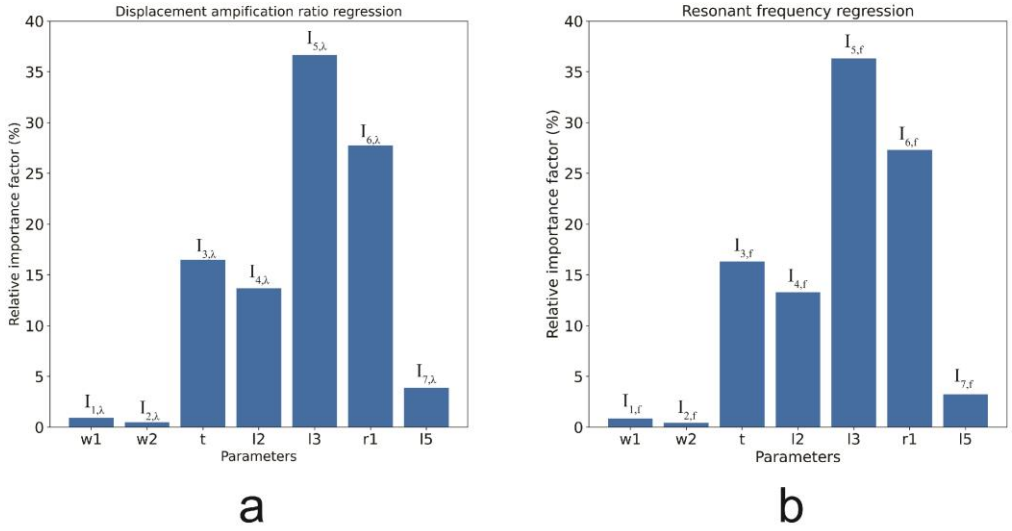

Fig 3: Relative importance factor of the seven variables in estimating (a) displacement amplification ratio and (b) resonant frequency.

Fig 3 (a) and (b) depict the percentage of relative importance factors; according to this figure, the effect of w_1, w_2, and l_5 on λ and f are less than 5%. The fixed values of these parameters are noted in Table 1. Also, the extended lower and upper limits for r_1, l_2, l_3 and t that participate in the optimization process, as well as the overall step size, are shown in Table 2. It should be noted that some combinations of the parameters in this region are infeasible and cannot be manipulated. The blue plane shown in Fig 4 is this geometric constraint. By eliminating these points (red dots left side of the plane) from the dataset, 460 points remain that can be used in the training, testing, and validation of the DNNs.

Table 1: The fixed geometric parameters of the parallel compliant mechanism.

parameter	w_1 (mm)	w_2 (mm)	ll (mm)	gap (mm)	l_1 (mm)	l_5 (mm)
value	18	8	1.5	0.6	1.75	31.25

Table 2: Expanded lower and upper bounds of selected variables, as well as the overall step size.

parameter	r_1 (mm)	l_2 (mm)	l_3 (mm)	t (mm)
lower bound	2	9	9	0.5
upper bound	3.5	33	33	0.55
overall step size	0.5	6	6	0.125

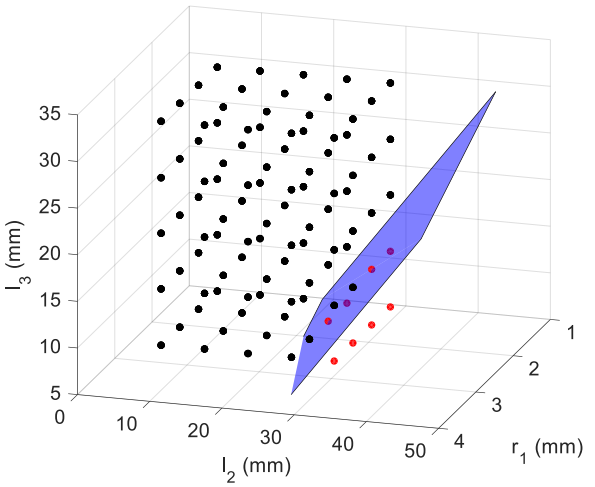

Fig 4: One fifth of the proposed dataset in the space of r_1, l_2, l_3 parameters. Four other similar sets points collected based on variation in t . Physically inconsistent points have been shown in red color and will be eliminated from the dataset for the subsequent studies.

2.3. Stiffness and compliance modeling

Although the sensitivity analysis is based on resonant frequency and displacement amplification ratio, stiffness is also required for defining a comprehensive criterion for evaluating the maximum working range of the mechanism. The linear force-displacement equation of the piezoelectric actuator is plotted in Fig 5 by two known points in displacement-force plane: (x_f , 0) and (0, F_b) which are characteristic properties of the piezo. Also, for the compliant mechanism, the linear force-displacement equation at the input plates (see Fig 2) passes through the origin with a slope of the input stiffness (k_{input}) . Therefore, the maximum accessible displacement at the piezoelectric actuator (x_s), can be obtained from the intersection of the two lines. On the other hand, the compliant mechanism output working range (X_s) could be calculated with the following equation:

$$X_s = \lambda x_s = \lambda \frac{F_b}{\lambda k_{input} + \frac{F_b}{x_f}} \tag{5}$$

According to Fig 5, a stiff mechanism may reduces piezoelectric elongation even if it has higher natural frequency, resulting in insufficient working range on the output stage even with a large amplification ratio.

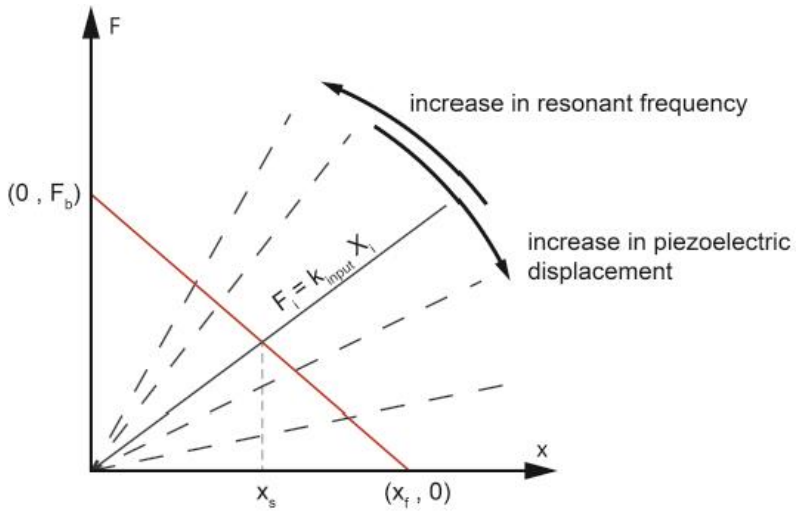

Fig 5: Characteristic force-displacement equations of the piezoelectric actuator and the compliant mechanism.

A compliance-based matrix method is also used in this study to develop an analytical model for couple hinges around the inner stage. We used Koseki's compliance matrices [37] for circular hinges and attached prismatic beams and followed the method proposed by Pham [38] for modeling the couple hinge. The relationship between loads and displacement at the end of both a prismatic beam and a circular hinge can be obtained as:

$$\varepsilon = \mathbf{C}F_i \tag{6}$$

with

$$\varepsilon_i = \left[d_x d_y \theta_z \right]^T ; F_i = \left[f_x f_y m_z \right]^T$$

where d_x, d_y, and θ_z are the displacement, and f_x, f_y, and m_z are the forces and moment, respectively, at the free end of the prismatic beam and circular hinge. The 3×3 compliance matrix of the prismatic beam and the circular hinge can be written as equations 7 and 8, respectively [38].

$$\mathbf{C}_{l,b} = \begin{bmatrix} \frac{1}{Eab} & 0 & \frac{6l^2}{Ea^3b} \\ 0 & \frac{4l^3}{Ea^3b} & 0 \\ \frac{6l^2}{Ea^3b} & 0 & \frac{12l}{Ea^3b} \end{bmatrix} \tag{7}$$

$$\mathbf{C}_{l,h} = \begin{bmatrix} -\frac{1}{Eb}\left(\frac{\pi}{2} - \pi\left(\frac{r}{t}\right)^{1/2}\right) & 0 & \frac{9\pi r^{3/2}}{2Ebt^{5/2}} \\ 0 & \frac{4l^3}{Ea^3b} & 0 \\ \frac{9\pi r^{3/2}}{2Ebt^{5/2}} & 0 & \frac{9\pi r^{1/2}}{2Ebt^{5/2}} \end{bmatrix} \tag{8}$$

For discussed mechanism, $r = r_1, a = 2r_1 + t, l = l_2$ or l_3, and b is the thickness of the aluminium sheet.

The compliance matrix of i[th] couple hinge $\left(\mathbf{C}_{couple,i}\right)$ can obtain after transferring and assembling the local compliance matrices as:

$$\mathbf{C}_{couple,i} = \mathbf{J}_i \mathbf{C}_i \mathbf{J}_i^T \tag{9}$$

Which $\mathbf{J}_i$ is the Jacobian matrix of the i[th] group of the hinges and beams and composed of 3×3 matrices that transfer local compliance of hinges and beams, and $\mathbf{C}_i$ is diagonal matrix of the $\mathbf{C}_{l,b}$ and $\mathbf{C}_{l,h}$. Fig 6 shows equivalent springs ($K_{couple,i}, i = 1,2,3,4,5,6$) around the inner stage that can be obtained by inversing the corresponding compliance matrix $(\mathbf{C}_{couple,i})$. According to the equilibrium in X-axis, the mathematical relation between the output displacement (X_S) and the displacement just after the amplifier part (x_O in Fig 2) can be written as:

$$\mathbf{K}_{couple,6,x}(X_S - x_O) + \mathbf{K}_{couple,5,x}(X_S - 0) + \mathbf{K}_{eq,1,2,x}(X_S - 0) + \mathbf{K}_{eq,3,4,x}(X_S - 0) = 0 \tag{10}$$

In which:

$\mathbf{K}_{couple,i,x}, i = 1,2,3,4,5,6$: X component of the i[th] couple hinge's stiffness matrix

$\mathbf{K}_{eq,i,j,x}, (i,j) = (1,2),(3,4)$: X component of the equivalent stiffness of $\mathbf{K}_{couple,i}$ and $\mathbf{K}_{couple,j}$

As an example, the stiffness matrix of the second spring ($\mathbf{K}_{couple,2}$) can be obtained equal to:

$$\mathbf{K}_{couple,6,x}(X_S - x_O) + \mathbf{K}_{couple,2} = \begin{bmatrix} 87603.429 & 0 & -396.376 \\ 0 & 20.271 & 0 \\ -396.376 & 0 & 5275657.859 \end{bmatrix} \tag{11}$$

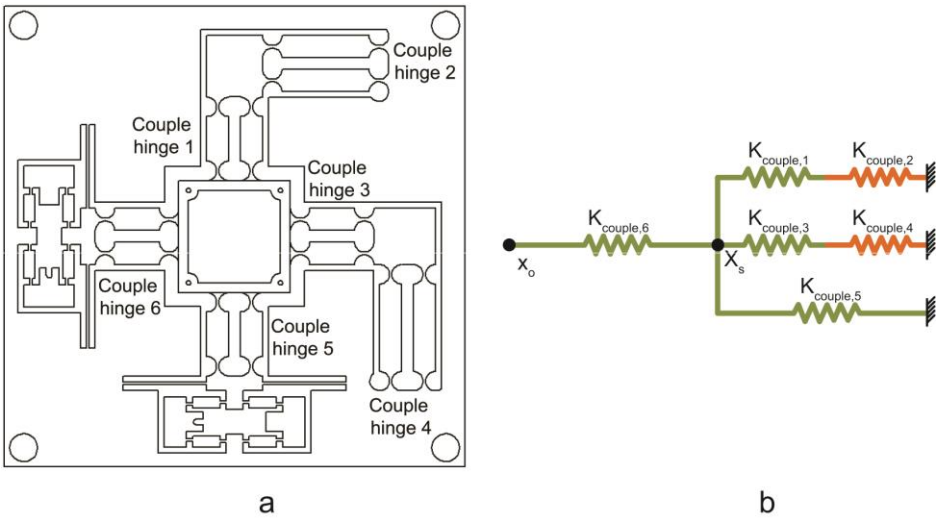

Fig 6: Couple hinges around the output stage (a) schematic model (b) lumped model.

Considering above equations, the proportion of x_O and X_S (displacements at the left and right ends of the

couple hinge 6 respectively) is equal to 0.999, which is quite close to the FEM simulation result (0.998).

2.4. Deep Neural Network (DNN)

A DNN comprises three types of layers: an input, a hidden, and an output layer. Each layer contains neurons that are fully interconnected with weights and biases. Neural networks estimate the relationship between inputs and outputs by adjusting the weights between neurons. The number of neurons in the input layer should be equal to the number of features in the dataset. The output layer shows the predicted displacement or principle resonant frequency of the mechanism. Hidden layers are layers with neurons that connect the input layer with the output layer; each layer receives the output of the previous layer as its input. Output of the i[th] neuron in the $(L+1)^{th}$ layer is calculated as follows [30]:

$$a_i^{L+1} = f(W_i^{L+1} Z^L + b_i^{L+1}) \tag{12}$$

where f is nonlinear activation function, $W_i^{L+1} = \{w_{1i}, w_{2i}, w_{3i}, ..., w_{ni}\}$ is the weights vector, in which n is the number of neurons in the L^{th} layer, $z^L = \{z_1, z_2, z_3, ..., z_n\}^T$ defines the output signal vector in the previous layer and b_i^{L+1} is the bias of the i^{th} neuron in the $(L+1)^{th}$ layer.

The number of layers, activation function, optimizer, and learning rates all affect performance of the DNN. In this study, four typical activation functions, including Sigmoid, Tanh, Rectified Linear Unit (ReLU) [39], and Exponential Linear Unit (ELU) [40] have been examined to determine the output signal of each neuron. The input parameters are standardized before feeding them to the DNN since they are within different ranges. Also, a mini-batch of 16 is employed to reduce the computational costs and root mean square error (RMSE) is used as an evaluation metric [35].

$$RMSE = \sqrt{\frac{1}{N}\left(\sum_{i=1}^{N} (z_i - \hat{z}_i)^2\right)} \tag{13}$$

where N is the number of training samples, z_i and $\hat{z}_i$ are the real and predicted values of the $(i)^{th}$ sample, respectively.

Back-propagation algorithm updates interconnection weights and biases to minimize the evaluation metric and two sets, test and validatopn, were used to evaluate the network performance. Accordingly, there are two different DNNs with four inputs and one output for working range and principle resonant frequency prediction.

2.5. Particle Swarm Optimization (PSO)

In PSO, instead of using more traditional genetic operators, each particle adjusts its movement based on its own experience as well as the experience of its neighbors. First, a population of particles is initialized with random positions and velocities, and a function is evaluated using its position as input. With each iteration, velocity (v_{id}) and position (x_{id}) of the particle are updated by [34]:

$$v_{id} = \omega v_{id} + c_1 r_1 (p_{id} - x_{id}) + c_2 r_2 (p_{gd} - x_{id}) \tag{14}$$

$$x_{id} = x_{id} + v_{id} \tag{15}$$

where $d = 1, 2, 3, ..., n$ represents the dimension, and $i = 1, 2, 3, ..., S$ denotes the particle index, S is the size of the swarm. Also, p_{id} is the previously best-visited position of $(i)^{th}$ particle and p_{gd} is the best particle in the

swarm, c_1 and c_2 are constants called cognitive and social scaling parameters, respectively. Moreover, r_1 and r_2 are random numbers drawn from a uniform distribution and ω is inertia weight that is used to control the velocity. These adjustments to the particle movement through the space cause it to search around the two best positions.

As the next step, both the particle memory and the best particle's archive are updated for the particles in the swarm. Fig 7 shows the schematic of the metamodeling and the optimization sections in more detail. The optimization goal of this study is to search for the best combination of geometric parameters to maximize the working range and the principle resonant frequency simultaneously. However, as discussed in section 2.3, this is not possible; Therefore, a single-objective constrained particle swarm optimization (SOCPSO) algorithm is used to maximize the principle natural frequency at a specific working range.

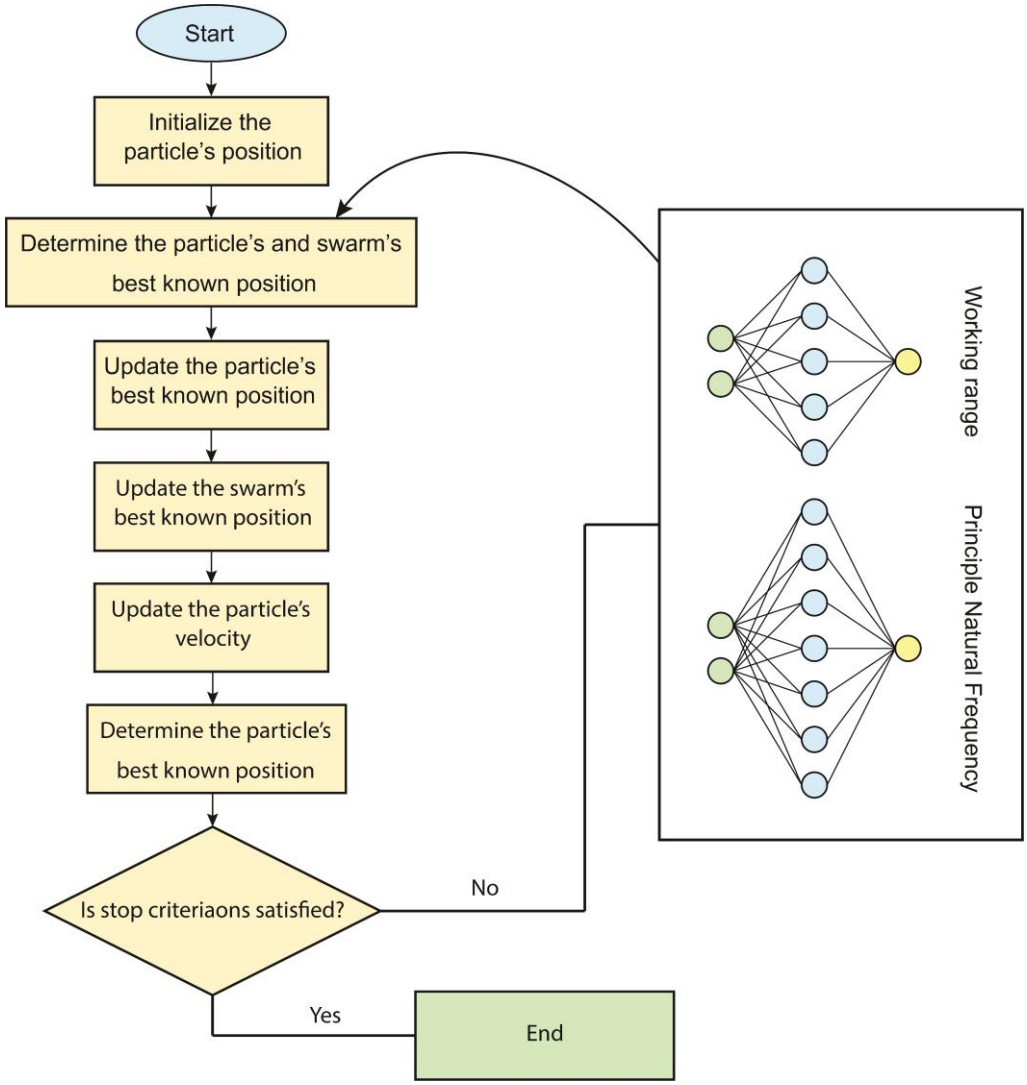

Fig 7: Schematic of the metamodel and the optimization algorithm.

3. Results and discussion

3.1. Deep neural network

3.1.1. Data acquisition

Fig 8 (a) and (b), respectively, show the change in the maximum working range and the principle resonant frequency for one-fifth of the dataset as a result of the variation of three geometric parameters, including $r_1, l_2, l_3 (t = 0.5mm)$. The outcomes in Fig 9 also reveal that the increase of t by keeping the other values constant

leads to a steep diminishing in the working range and an increase in the principle resonant frequency as well as the stiffness of the compliant mechanism, just in contrast to the other parameters discussed. These findings were expected from equations 7 and 8; according to these relations, an increase in r_1 and l_3 would amplify the compliance of prismatic beams and the circular hinges in the mechanism. A similar effect is also seen on leaf spring compliance when l_2 is increased. On the other hand, thickening the mechanism (increase in t) reduces the compliance of all three mentioned parts. This figure also shows the intrinsic trade-off between the displacement magnification and the resonant frequency which is a principle in designing compliant mechanisms.

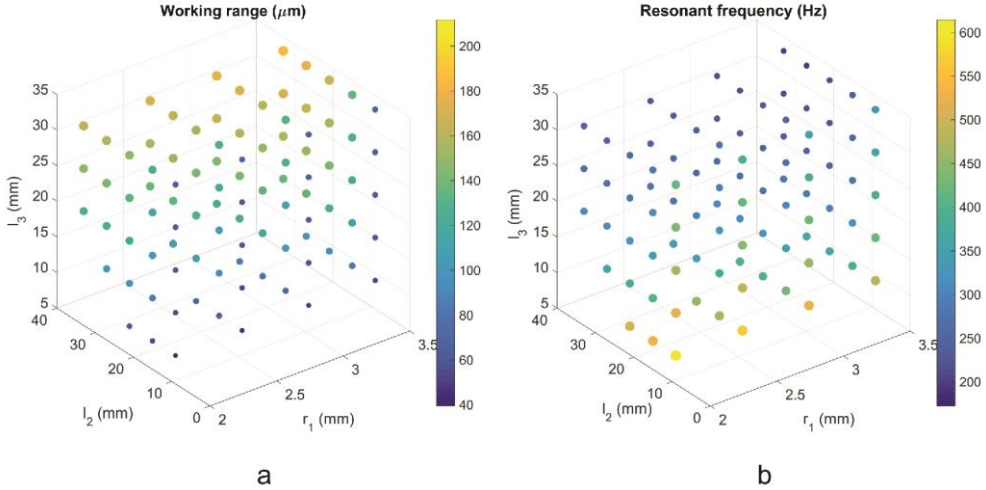

Fig 8: Variation of the (a) working range and (b) principle natural frequency of the proposed dataset in the variables space.

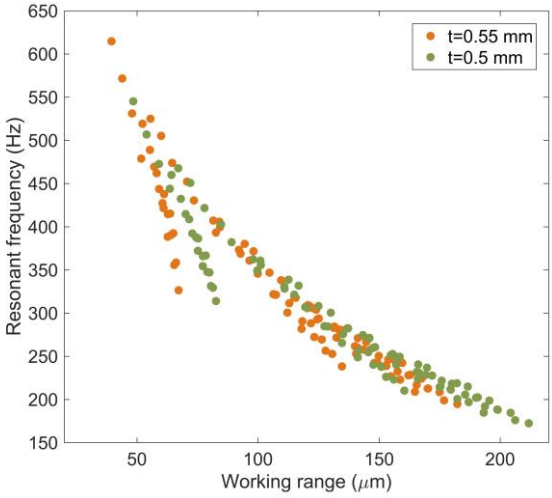

Fig 9: Effect of change of parameter t on the working range and the principle natural frequency of the mechanism.

3.1.2. Deep neural network architecture

The proposed dataset is split into the three training, validation, and test sets with a ratio of 0.6, 0.15, and 0.25, respectively. First, to achieve the best performance, the combination of activation and optimizer for each DNN is determined based on the results of several tests. Therefore, various activation functions and optimization algorithms are performed to identify the best combination of the activation function and optimizer to train the network.

There are 28 different combinations of four activation functions (e.g., ReLU, Elu, Tanh, Sigmoid) and seven optimizers (e.g., Adamax, Adam, RMSprop, SGD, Adadelta, Adagrad, Nadam). Two 4-10-10-1 architectures are trained with different activation functions and optimizers after 5000 epochs for working range and, resonant frequency. As shown in Table 3, for the working range, the combination of Elu and Adamax and, for the resonant frequency, the combination of Tanh and Adamax have the smallest RMSE for the training and testing sets.

Table 3: RMSE of different combinations of optimizers and activation functions for prediction of working range (W.R.) and resonant frequency (f) for validation (Val.) and test datasets after 5000 epochs.

Activation function			Relu		Elu		Tanh		Sigmoid	
RMSE			Val.	test	Val.	test	Val.	test	Val.	test
Optimizer	Adamax	W.R.	1.5762	1.3131	0.3487	0.3378	0.5268	0.5483	0.3687	0.3807
		f	3.1044	2.9688	2.5789	2.4659	1.9543	1.3278	2.6522	2.2836
	Adam	W.R.	1.5974	1.2475	0.5085	0.543	0.8958	0.827	1.433	0.7055
		f	2.9334	3.2543	2.0161	2.2744	4.427	3.1213	2.7601	2.7745
	RMSProp	W.R.	4.254	4.1823	9.0318	8.7034	10.8521	11.7169	13.2717	11.4614
		f	8.1782	8.2814	34.958	35.2299	91.361	86.4904	24.442	23.1106
	SGD	W.R.	43.7826	34.118	Nan	Nan	38.1239	34.118	19.6711	20.1932
		f	91.0238	86.4042	Nan	Nan	86.5319	84.1498	91.1427	88.658
	Adadelta	W.R.	20.5351	19.7992	16.1297	16.4467	98.8272	93.5416	78.0491	72.807
		f	35.5715	34.4568	44.4493	42.5801	274.7921	281.773	170.0011	175.4132
	Adagrad	W.R.	11.6768	12.2862	4.6309	4.6105	76.4049	71.174	86.3279	81.0527
		f	18.7466	20.1875	27.5344	29.1217	254.7314	261.5358	258.6041	265.4452
	Nadam	W.R.	1.4927	1.1552	1.1137	1.0935	0.7174	0.6527	0.4379	0.4606
		f	4.16	3.5125	2.8801	2.8643	2.1334	1.9045	1.9999	1.6321

Therefore, the combination of the Adamax algorithm with 0.01 learning rate and other default values for decay rate parameters with Elu and Tanh functions are employed to create two neural networks designed to predict the maximum working range and resonant frequency, respectively.

Thereafter, various numbers of hidden layers and units, shown in Table 4, are examined to determine the network size.

Table 4: Comparison of root mean square error of different neural network architectures for training and test datasets after 10000 epochs.

Architecture	W.R. (μm)		f (Hz)	
	Training	Test	Training	Test
4-15-1	1.3107	1.1974	-	-
4-20-1	0.4282	0.4683	1.9043	1.8908
4-10-10-1	0.3816	0.403	1.6	1.5544
4-15-15-1	0.2291	0.2301	2.1737	3.2999
4-20-20-1	0.2487	0.2596	1.5916	2.6503
4-25-25-1	-	-	2.5661	1.7708
4-30-30-1	0.3683	0.3626	2.2978	1.6748
4-50-50-1	-	-	3.344	1.82
4-20-20-20-1	0.3057	0.3229	2.7518	1.4829

3.1.3. Training results

In order to evaluate the performance of the networks, a fit model is used. The R-squared (R^2) value is used to show the correlation between predicted outputs and the real values, and mean absolute percent error (*MAPE*) that measures the size of error for the model in percentage terms, calculated through the following formulas:

$$R^2 = 1 - \frac{\sum_{i=1}^{N} (z_i - \hat{z}_i)^2}{\sum_{i=1}^{N} (z_i - \bar{z}_i)^2} \tag{16}$$

$$MAPE = \left(\frac{1}{N} \sum_{i=1}^{N} \frac{| z_i - \hat{z}_i |}{| z_i |} \right) \times 100 \tag{17}$$

where $\bar{z}_i$ is the mean of the values. Note that a higher value of R^2 means a more accurate mathematical model, while a higher $MAPE$ value refers to a less accurate one. Verification of the models is shown in Table 5 and Fig 10. These results indicate a good correlation between real values and models outputs especially for the resonant frequency network.

Table 5: The R-squared value and the mean absolute percent error of the networks

Model	R^2	MAPE
Working range network	0.9998	0.3387
Resonant frequency network	0.9999	0.1449

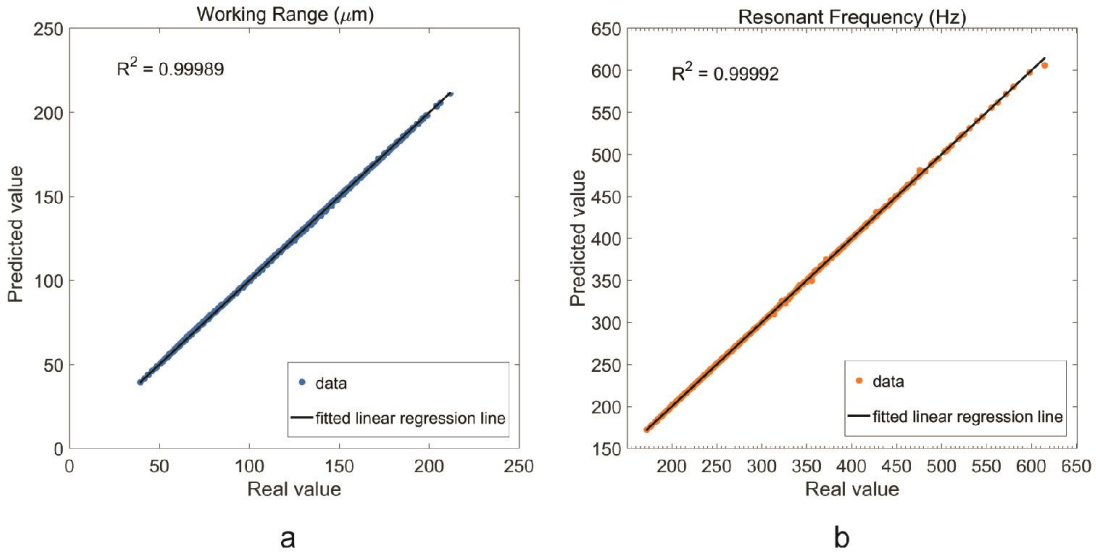

Fig 10: Verification of the models' behavior (a) working range network (b) resonant frequency network.

3.2. Single-objective constrained particle swarm optimization

In the preceding section, a deep neural network was presented as a metamodel for the finite element method and trained to predict the two deciding factors of the parallel compliant mechanism. Within this section, SOCPSO is employed as a strong algorithm to attain the highest principle resonant frequency while also ensuring the design's constraints, such as a minimum working range and geometric compatibility. In the optimization process, SOCPSO algorithm is executed for seven case studies with the minimum accepted working ranges of 110, 118, 118.5, 119, 119.5, 120, and 130 μm. In all cases, a population of 100 individuals starts with an initial point of $[r_1 = 3, l_2 = 33, l_3 = 33, t = 0.5]$ with objective function value of 184.76 Hz and corresponding working range of 203. 34 μm tries to find the best solution. The objective function will be extremely penalized at unfeasible points (the right side of the plane in Fig 4).

Fig 11 illustrates the history of the objective function of particles through epochs. In the first generations, the particles are spread in space, and after a few generations, they move toward the best position of particles and search for a better solution. The algorithm stops searching when the best solution is not improved after a few successive generations and presents the optimum point. This figure also depicts a separation in the individuals' position caused

by the geometric constraint. The objective function of a fraction of the population has been penalized after violating the constraint and thus descended to negative values.

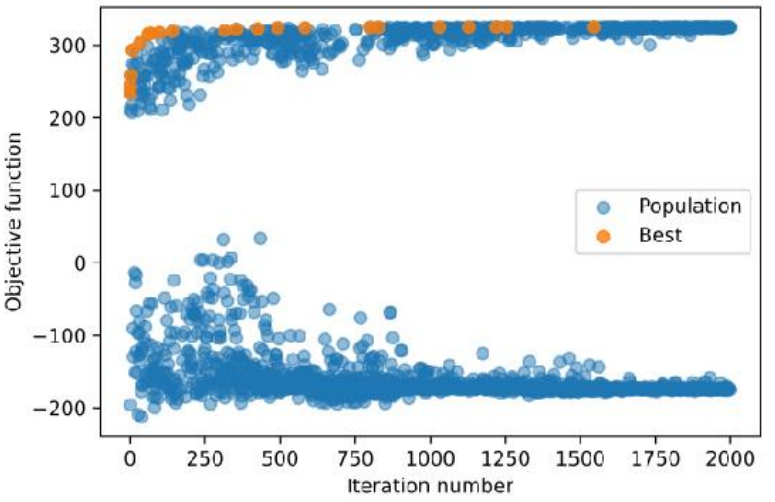

Fig 11: The history of the objective function evaluation in the optimization. The best individual of each generation is shown in the orange color.

Fig 12 depicts the working range and resonant frequency of the initial point, as well as the output of the PSO algorithm based on neural network metamodeling and FEM results used as the dataset. @R1_10 According to this figure, the optimization protocol has succeeded to find the optimum design even by using far away initial point. Characteristic parameters and coordination of these seven points are given in Table 6. According to the table, the proposed optimization guideline based on training the neural network on the reduced variations space can predict both the resonant frequency and the working range of the parallel compliant mechanism with an acceptable error. Moreover, it is shown that the lower $MAPE$ value for the resonant frequency network makes it more accurate than the working range network.

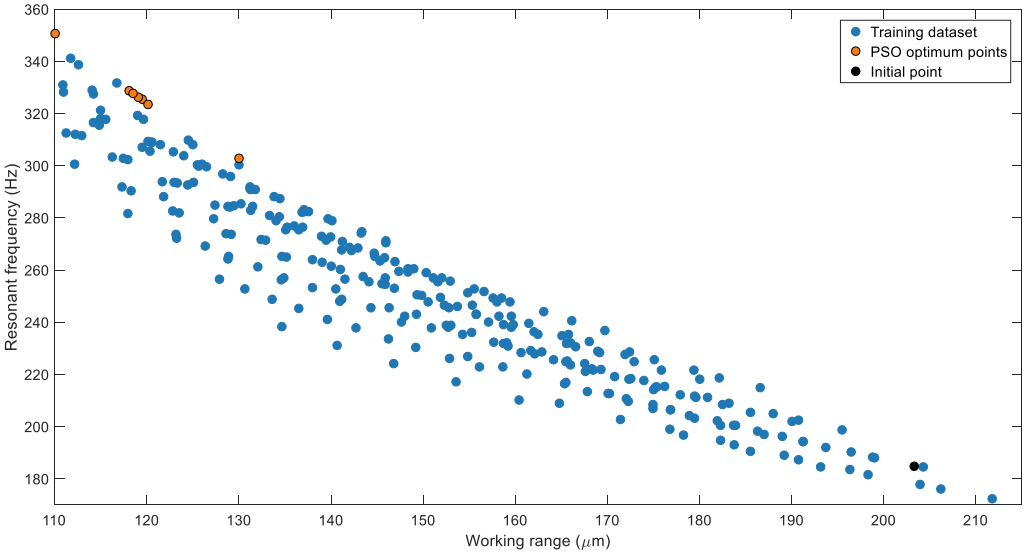

Fig 12: Predicted principle resonant frequencies by the proposed guideline for a desirable working range of 110, 118, 118.5, 119, 119.5, 120, and 130 μm (orange dots) in comparison with the FEM simulation of the training dataset (blue dots) and PSO initial point (black dot).

For the fifth case study, seven different starting points are used to investigate the optimization protocol performance; As shown in Table 7, although the optimal location varies based on the initial guess, the values of the objective function at these points are quite close to each other. Also, this table shows that the algorithm can reach the optimal point for all considered initial guesses in a limited number of iterations.

3.3. Results verification

In order to ensure the applicability of the optimization scheme, the accuracy of the predicted optimum combination of the resonant frequency and the maximum working range should be examined by FEM. Fig 13 depicts the average displacement of 118.76 μm in the inner stage with amplification ratios of 5.615 in the X direction for a force of 286 N exerted by the vertical piezoelectric, corresponding to the fifth case study in Table 6. As expected, leaf springs act as a motion decoupler, and reduce the cross-coupling to less than 0.2% which agrees with the work of Lee et al. [26]. With a similar simulation, the maximum working range also for the Y direction is calculated at 119.50 μm which has a good agreement with the X direction thanks to the symmetric topology. Also, the maximum Von Mises stress in the mechanism is obtained equal to 138.586 MPa, which can ensure a good fatigue life due to the fatigue strength of Al 7075-T6 (159 MPa). In addition, the principle natural frequency of the mechanism is 327.5377 Hz along the X-axis with just 0.65% error with the prediction of the DNN. Another in-plane mode is measured at 383.09 Hz. The third and fourth modes are out of the plane and equal 479.97 Hz and 536.31 Hz, respectively. It is worth noting that Table 6 shows the novel optimization protocol developed in this research could find some better combinations of working range and resonant frequency rather than what was proposed before for a similar geometry by Lee et al. [26]. More specifically, the fifth case in this table notes that for an equal desired working range, at least one configuration of geometric parameters is found with a higher resonant frequency than 278.9 Hz in Lee's work [26]. This comparison shows that using a robust metamodel as an alternative to FEM can find practical solutions that were previously missed in the traditional time-consuming method.

Table 6: A comparison of the predicted working range and the resonant frequency by the neural networks and the real values, obtained by applying the Finite Element Method to the seven optimum problem cases

Case number	Position				PSO outputs		FEM verification		error (%)	
	$r_1(mm)$	$l_2(mm)$	$l_3(mm)$	$t(mm)$	W.R. $(\mu m)\ \mu m$	f (Hz)	W.R. (μm)	f (Hz)	W.R. $(\mu m)\ \mu m$	f (Hz)
1	2	28.18	13.52	0.5	110.00	350.71	107.29	351.47	2.527	0.215
2	2.23	27.65	13.90	0.5	118.06	328.67	115.79	329.93	1.953	0.380
3	2.21	29.32	13.98	0.5	118.51	327.65	116.35	329.80	1.856	0.650
4	2.30	28.20	13.73	0.5	119.03	326.24	116.99	327.23	1.744	0.303
5	2	31.05	15.09	0.5	119.50	325.41	118.82	327.54	0.575	0.650
6	2	30.48	15.23	0.5	120.10	323.64	119.52	326.53	0.484	0.883
7	2	33	17.10	0.5	130.00	302.82	131.80	304.10	1.365	0.423

Table 7: PSO output for desired working range of 119.5 $\mu m\ \mu m$ for different initial points

Initial point				Iterations	PSO optimum				f (Hz)	W.R. (μm)
$r_1(mm)$	$l_2(mm)$	$l_3(mm)$	$t(mm)$		$r_1(mm)$	$l_2(mm)$	$l_3(mm)$	$t(mm)$		
3	33	33	0.5	41	2	31.086	15.088	0.5	325.41	119.50
3	33	33	0.55	22	2	28.20	15.1	0.5	325.41	119.50
3	30	30	0.5	8	2	30.67	15.12	0.5	325.35	119.51
3.5	33	33	0.55	9	2	30.11	15.17	0.5	325.24	119.54
2.5	30	30	0.55	14	2	28.84	15.26	0.5	325.20	119.51
2.5	27	27	0.55	7	2	27.56	15.38	0.5	324.83	119.60
3	20	20	0.5	41	2	31.087	15.088	0.5	325.41	119.50

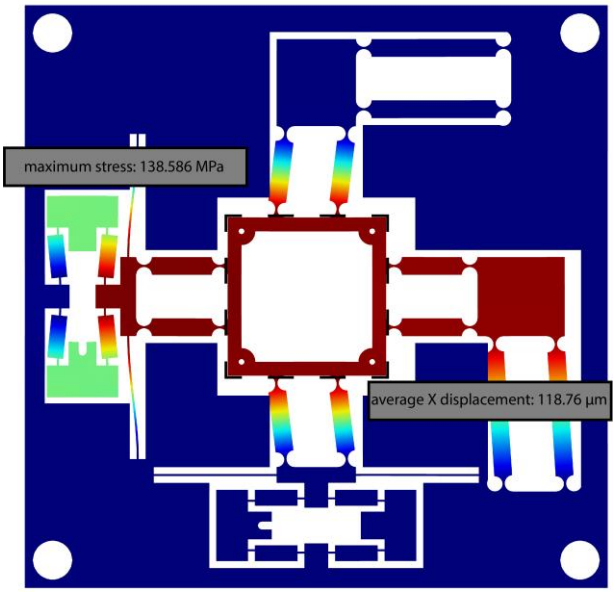

Fig 13: The working range of 118.7 μm at the inner stage in the X-axis for case study number 5 by applying the Finite Element Method.

4. Conclusion

Geometric optimization is an imperative step in designing (2-DOF) compliant positioners to obtain the desired performance. This study presented a thorough guideline for optimizing compliant mechanisms to increase the resonant frequency and working range simultaneously using a neural network that is consistent with finite element analysis and analytical modeling. The proposed optimization procedure can move toward the desired regardless of the initial point and riches the optimum point in a few iterations. To be concluded, it could be noted:

- ✓ For the parallel compliant mechanism shown in Fig 2, only four geometric parameters significantly affect the performance of the mechanism.
- ✓ The maximum working range of the compliant positioner is determined not only by λ but also relies on the stiffness of the stage and piezo stack.
- ✓ Using a smart data selection method provides robust neural network learning and achieves high-accuracy prediction with a relatively small dataset.
- ✓ The final proposed design shows an improvement of 17% in resonant frequency compared to a similar design in the literature.

Advantages:

The presented study on the compliant mechanism optimization process has the advantages listed below:

- ✓ The proposed sensitivity analysis advance the optimization process by speeding up the DNN's training.
- ✓ Once the models have been trained, the optimization process can be repeated for various desired working ranges or resonant frequencies with neglectable computational costs.
- ✓ DNN metamodeling enables designers to find optimal designs that are usually missed by FEA because of the high computation costs.
- ✓ The proposed guideline reduces the computation time of the compliant mechanism's optimization by an order of 100 by using neural network metamodels instead of FEM analysis.

Limitations:

The following limitations can be attributed to the presents study:

- ✓ Maximum stress in the structure and the cross-coupling of the two axes are some of the most important parameters which are not considered in the presented protocol. Specifically, using DNNs for taking stress into account in compliant mechanisms optimization is recommended to be followed as a future study.
- ✓ In order to avoid potential incompatibility, geometric and manufacturing constraints must be expressed explicitly. (this limitation also exists in the traditional method)
- ✓ The proposed optimization method is highly dependent on dimension reduction; therefore, it is important to ensure the proper sensitivity analysis before starting the optimization.

References

[1] W. Dong, F. Chen, F. Gao, M. Yang, L. Sun, Z. Du, J. Tang, D. Zhang, Development and analysis of a bridge-lever-type displacement amplifier based on hybrid flexure hinges, *Precision Engineering*, Vol. 54, pp. 171-181, 2018.

[2] S. Iqbal, A. Malik, A review on MEMS based micro displacement amplification mechanisms, *Sensors and Actuators A: Physical*, Vol. 300, pp. 111666, 2019.

[3] J. Wei, S. Fatikow, X. Zhang, O. C. Haenssler, Design and experimental evaluation of a compliant mechanism-based stepping-motion actuator with multi-mode, *Smart Materials and Structures*, Vol. 27, No. 10, pp. 105014, 2018.

[4] M. Ling, X. Zhang, Coupled dynamic modeling of piezo-actuated compliant mechanisms subjected to external loads, *Mechanism and Machine Theory*, Vol. 160, pp. 104283, 2021.

[5] P. Gräser, S. Linß, F. Harfensteller, M. Torres, L. Zentner, R. Theska, High-precision and large-stroke XY micropositioning stage based on serially arranged compliant mechanisms with flexure hinges, *Precision Engineering*, 2021.

[6] W.-L. Zhu, Z. Zhu, P. Guo, B.-F. Ju, A novel hybrid actuation mechanism based XY nanopositioning stage with totally decoupled kinematics, *Mechanical Systems and Signal Processing*, Vol. 99, pp. 747-759, 2018.

[7] L. L. Howell, *Compliant mechanisms*, in: *21st century kinematics*, Eds., pp. 189-216: Springer, 2013.

[8] L. Zentner, S. Linß, 2019, *Compliant systems: Mechanics of elastically deformable mechanisms, actuators and sensors*, Walter de Gruyter GmbH & Co KG,

[9] M. Ling, J. Cao, M. Zeng, J. Lin, D. J. Inman, Enhanced mathematical modeling of the displacement amplification ratio for piezoelectric compliant mechanisms, *Smart Materials and Structures*, Vol. 25, No. 7, pp. 075022, 2016.

[10] X. Xi, T. Clancy, X. Wu, Y. Sun, X. Liu, A MEMS XY-stage integrating compliant mechanism for nanopositioning at sub-nanometer resolution, *Journal of Micromechanics and Microengineering*, Vol. 26, No. 2, pp. 025014, 2016.

[11] Y. K. Yong, S. S. Aphale, S. R. Moheimani, Design, identification, and control of a flexure-based XY stage for fast nanoscale positioning, *IEEE Transactions on Nanotechnology*, Vol. 8, No. 1, pp. 46-54, 2008.

[12] P. Wang, Q. Xu, Design and testing of a flexure-based constant-force stage for biological cell micromanipulation, *IEEE Transactions on automation science and engineering*, Vol. 15, No. 3, pp. 1114-1126, 2017.

[13] T. K. Das, B. Shirinzadeh, M. Ghafarian, A. Al-Jodah, Design, analysis, and experimental investigation of a single-stage and low parasitic motion piezoelectric actuated microgripper, *Smart Materials and Structures*, Vol. 29, No. 4, pp. 045028, 2020.

[14] Y.-l. Yang, Y.-d. Wei, J.-q. Lou, G. Tian, X.-w. Zhao, L. Fu, A new piezo-driven microgripper based on the double-rocker mechanism, *Smart Materials and Structures*, Vol. 24, No. 7, pp. 075031, 2015.

[15] T. Jin, S. Luo, Y. Le, J. Wu, L. Lei, B. Zhang, Design and analysis of a low crosstalk error nested structure two-dimensional micro-displacement stage, *Advances in Mechanical Engineering*, Vol. 13, No. 4, pp. 16878140211014061, 2021.

[16] Z. Wu, Q. Xu, Design, optimization and testing of a compact XY parallel nanopositioning stage with stacked structure, *Mechanism and Machine Theory*, Vol. 126, pp. 171-188, 2018.

[17] Q. Xu, Design and development of a compact flexure-based $ XY $ precision positioning system with centimeter range, *IEEE Transactions on Industrial Electronics*, Vol. 61, No. 2, pp. 893-903, 2013.

[18] C.-X. Li, G.-Y. Gu, M.-J. Yang, L.-M. Zhu, Design, analysis and testing of a parallel-kinematic high-bandwidth XY nanopositioning stage, *Review of Scientific instruments*, Vol. 84, No. 12, pp. 125111, 2013.

[19] S. P. Wadikhaye, Y. K. Yong, S. R. Moheimani, A novel serial-kinematic AFM scanner: design and characterization, in *Proceeding of*, IEEE, pp. 50-55.

[20] B. J. Kenton, K. K. Leang, Design and control of a three-axis serial-kinematic high-bandwidth nanopositioner, *IEEE/ASME Transactions on Mechatronics*, Vol. 17, No. 2, pp. 356-369, 2011.

[21] H. Tang, Y. Li, J. Huang, Design and analysis of a dual-mode driven parallel XY micromanipulator for micro/nanomanipulations, *Proceedings of the Institution of Mechanical Engineers, Part C: Journal of Mechanical Engineering Science*, Vol. 226, No. 12, pp. 3043-3057, 2012.

[22] N. Hosseini, A. Nievergelt, J. Adams, V. Stavrov, G. Fantner, A monolithic MEMS position sensor for closed-loop high-speed atomic force microscopy, *Nanotechnology*, Vol. 27, No. 13, pp. 135705, 2016.

[23] Q. Yao, J. Dong, P. M. Ferreira, Design, analysis, fabrication and testing of a parallel-kinematic micropositioning XY stage, *International Journal of Machine Tools and Manufacture*, Vol. 47, No. 6, pp. 946-961, 2007.

[24] F. Wang, X. Zhao, Z. Huo, B. Shi, C. Liang, Y. Tian, D. Zhang, A 2-DOF nano-positioning scanner with novel compound decoupling-guiding mechanism, *Mechanism and Machine Theory*, Vol. 155, pp. 104066, 2021.

[25] Y. Li, Q. Xu, A novel piezoactuated XY stage with parallel, decoupled, and stacked flexure structure for micro-/nanopositioning, *IEEE Transactions on Industrial Electronics*, Vol. 58, No. 8, pp. 3601-3615, 2010.

[26] H.-J. Lee, S. Woo, J. Park, J.-H. Jeong, M. Kim, J. Ryu, D.-G. Gweon, Y.-M. Choi, Compact compliant parallel XY nano-positioning stage with high dynamic performance, small crosstalk, and small yaw motion, *Microsystem Technologies*, Vol. 24, No. 6, pp. 2653-2662, 2018.

[27] Y. Tian, Y. Ma, F. Wang, K. Lu, D. Zhang, A novel XYZ micro/nano positioner with an amplifier based on L-shape levers and half-bridge structure, *Sensors and Actuators A: Physical*, Vol. 302, pp. 111777, 2020.

[28] Y. Qin, B. Shirinzadeh, Y. Tian, D. Zhang, Design issues in a decoupled XY stage: Static and dynamics modeling, hysteresis compensation, and tracking control, *Sensors and Actuators A: Physical*, Vol. 194, pp. 95-105, 2013.

[29] J. Ferreiro-Cabello, E. Fraile-Garcia, E. M. de Pison Ascacibar, F. Martinez-de-Pison, Metamodel-based design optimization of structural one-way slabs based on deep learning neural networks to reduce environmental impact, *Engineering Structures*, Vol. 155, pp. 91-101, 2018.

[30] T. T. Truong, J. Lee, T. Nguyen-Thoi, Multi-objective optimization of multi-directional functionally graded beams using an effective deep feedforward neural network-SMPSO algorithm, *Structural and Multidisciplinary Optimization*, Vol. 63, No. 6, pp. 2889-2918, 2021.

[31] D. Bielecki, D. Patel, R. Rai, G. F. Dargush, Multi-stage deep neural network accelerated topology optimization, *Structural and Multidisciplinary Optimization*, Vol. 64, No. 6, pp. 3473-3487, 2021.

[32] C. Qian, W. Ye, Accelerating gradient-based topology optimization design with dual-model artificial neural networks, *Structural and Multidisciplinary Optimization*, Vol. 63, No. 4, pp. 1687-1707, 2021.

[33] J. Kennedy, R. Eberhart, Particle swarm optimization, in *Proceeding of*, IEEE, pp. 1942-1948.

[34] J. C. Bansal, P. Singh, M. Saraswat, A. Verma, S. S. Jadon, A. Abraham, Inertia weight strategies in particle swarm optimization, in *Proceeding of*, IEEE, pp. 633-640.

[35] Z. Zhao, Z. Chen, S. Liu, Hybrid FEM-ANN-PSO Method To Optimize The Structural Parameters Of Wafer-Level Chip Scale Package (WLCSP) For High Reliability, in *Proceeding of*, IEEE, pp. 1-5.

[36] H.-W. Ma, S.-M. Yao, L.-Q. Wang, Z. Zhong, Analysis of the displacement amplification ratio of bridge-type flexure hinge, *Sensors and Actuators A: Physical*, Vol. 132, No. 2, pp. 730-736, 2006.

[37] Y. Koseki, T. Tanikawa, N. Koyachi, T. Arai, Kinematic analysis of a translational 3-dof micro-parallel mechanism using the matrix method, *Advanced Robotics*, Vol. 16, No. 3, pp. 251-264, 2002.

[38] H.-H. Pham, I.-M. Chen, Stiffness modeling of flexure parallel mechanism, *Precision Engineering*, Vol. 29, No. 4, pp. 467-478, 2005.

[39] V. Nair, G. E. Hinton, Rectified linear units improve restricted boltzmann machines, in *Proceeding of*.

[40] D.-A. Clevert, T. Unterthiner, S. Hochreiter, Fast and accurate deep network learning by exponential linear units (elus), *arXiv preprint arXiv:1511.07289*, 2015.